Prediction of long-term extreme load effects due to wave and wind actions for cable-supported bridges with floating pylons

Yuwang Xu[a1], Ole Øiseth[a], Torgeir Moan[b], Arvid Naess[c]

a Department of Structural Engineering, Norwegian University of Science and Technology, Richard Birkelands vei 1, Trondheim, Norway

b Centre for Autonomous Marine Operations and Systems, Centre for Ships and Ocean Structures, Norwegian University of Science and Technology, O. Nielsens v 10, Trondheim, Norway

c Department of Mathematical Sciences, Norwegian University of Science and Technology, Alfred Getz vei 1, Trondheim, Norway

Abstract

The characteristic values of the extreme environmental load effects should correspond to a specified annual probability of exceedance. These load effects can be calculated using short-term or long-term methods. The full long-term method is considered the most accurate approach, but it requires tremendous computational effort for complicated structures, especially when nonlinearities must be considered. In a case study of the dynamic behavior of a three-span suspension bridge with two floating pylons, these nonlinearities are found to have a significant effect on the extreme values of some of the load effects. It is thus recommended to determine these responses in the time domain. However, time domain simulations can be very time consuming even by using simplified approaches such as the environmental contour method (ECM) and the inverse first-order reliability method (IFORM). Therefore, this paper introduces a computationally efficient approach utilizing the ECM and the IFORM to determine long-term extreme values based on responses from combined frequency and time domain simulations.

Keywords:

[1] *Corresponding author. Tel.: +4740337211*

E-mail address: yuwang.xu@ntnu.no

cable-supported bridge, floating pylons, long-term extreme load effects, inverse first-order reliability method, environmental contour method

1. Introduction

During the design of offshore structures, it is necessary to estimate the characteristic values of extreme load effects corresponding to specified annual exceedance probabilities. These load effects are calculated using short-term or long-term methods. Short-term approaches are used to analyze load effects during storms with N-year return periods with specified durations, e.g., three hours for offshore structures subject to waves and normally one hour for structures experiencing combined wind and wave actions; meanwhile, long-term approaches consider all storms that occur in the long-term period.

In principle, the full long-term methods (FLM) represents the most accurate approaches for determining the characteristic values of extreme load effects on a structure for ultimate limit state (ULS) and accidental limit state (ALS) design checks. In Norwegian rules and regulations [1], the ULS and ALS values normally correspond to annual exceedance probabilities of 10^{-2} and 10^{-4}, respectively, for offshore structures. The FLM essentially integrates short-term response statistics (i.e., distributions of all peaks, distributions of extreme values or mean upcrossing rate) over all short-term environmental conditions [2]. It incorporates both the long-term variability of environmental conditions represented by a joint probability distribution of environmental parameters and the variability of short-term extreme values characterized by the conditional distribution of short-term responses with regard to the environmental conditions.

However, the FLM clearly does not represent the most economical approach from a computational perspective because they must account for contributions from all possible short-term states [3]. Determination of the annual probability of exceedance given a response is analogous to determining probability of failure (if failure is defined as exceeding a given response). Hence, structural reliability methods (e.g. FORM) [4-6] can be used to determine the distribution of long term extreme response values. If the annual probability of exceedance or return period is given, the inverse method (e.g. IFORM) [7-9] needs to be used.

The environmental contour method (ECM), which is a simplification of IFORM, decouples the uncertainty in the environmental conditions and the short-term extreme values and the latter is disregarded [10-13]. Fundamentally, the ECM calculates the contour line corresponding to a selected return period. It is further assumed that the most important combination of environmental parameters along the contour line can be used to approximate the long-term extreme value. Neglecting the short-term variability in the extreme values can give non-conservative results. Thus, a higher percentile than the expected maximum is used as the short-term characteristic value rather than selecting the median extreme response [10]. Another alternative is to introduce a correction factor that is typically between 1.1 and 1.3 to make the prediction conservative [13-15]. The ECM has been frequently applied in ocean engineering endeavors to search for the appropriate short-term design case. This method makes it possible to estimate the long-term extreme response without conducting a full long-term analysis, which is especially beneficial for complex structures.

To an extent, a simplified FLM can guarantee both accurate and computationally efficient results because not all of the conditions contribute to the long-term extreme value distribution [13]. It is therefore necessary to assess whether the environmental conditions yield significant contributions; if not, they could be disregarded. By determining an appropriate range for the environmental parameters, e.g., wind velocities, wave heights and peak periods, significant reduction of computational times can be achieved.

Most of the research so far is focusing on wave induced load effects for offshore structures, while there exist some studies on combined wind and wave load. This paper addresses a very complex structural response problem, i.e., a three-span suspension bridge with two floating pylons subjected to combined wind and wave loading. Three environmental parameters are considered, namely, the mean wind velocity, the significant wave height and the peak wave period. Due to their computational efficiency, frequency domain methods are normally the first choice for obtaining the structural response required for long-term extreme value analyses. The accuracy of the simplified FLM, ECM and IFORM is validated through a comparison with the results applying the FLM. The results show

that the simplified methods provide adequate results and can thus be used for predicting the wind- and wave-induced extreme load effects in this new bridge concept.

The time domain simulations presented demonstrate that nonlinearities constitute a difference of approximately 20% in the extreme values of the bending moment due to vertical deformation at the most important position along the girder. This means that frequency domain approaches may underestimate the long-term extreme response. However, time domain simulations can be very time consuming, even by applying the ECM or IFORM. Therefore, a computationally efficient approach is proposed to predict the long-term extreme response values based on the combined frequency and time domain simulation results and the use of IFORM and ECM. The idea of using IFORM arises from the observation in the case study that the search for the design point converges quickly and most of the iterations are located in a small area near the design point. Thus the domain of environmental parameters can be divided into a frequency domain region and time domain region. Time domain simulations are utilized only as the iteration is performed in the time domain region. The time domain region constitutes only a small percentage, which is the key to avoid tremendous computational time.

2. Dynamic response of a cable-supported bridge with floating pylons

Fig. 1. Three-span suspension bridge with two floating pylons. Illustrated by Arne Jørgen Myhre, Statens vegvesen

Fig. 1 shows a three-span suspension bridge with two floating pylons traversing Bjørnafjorden in Norway. The main cables are supported by two fixed pylons at each end of the bridge and two floating pylons in the middle. Similar to a tension leg platform, the bottom part of each floating pylon is moored by four groups of tethers that provide large stiffness coefficients for the heave, pitch and roll.

The water depths at the left and right floating pylons are 550 m and 450 m, respectively. The dynamic behavior of the bridge can be simulated through both time and frequency domain approaches [16, 17].

2.1 Multi-mode frequency domain approach

Since multi-mode approaches can consider aerodynamic coupling effects among the modes, they demonstrate better performance in predicting the buffeting responses of bridges relative to conventional mode-by-mode approaches [18, 19]. A cable-supported bridge with floating pylons experiences both wind and wave action, and the associated equation of motion can be written in the frequency domain as follows:

$$(\tilde{\mathbf{M}}_s + \tilde{\mathbf{M}}_h(\omega))\mathbf{G}_{\ddot{\boldsymbol{\eta}}}(\omega) + (\tilde{\mathbf{C}}_s + \tilde{\mathbf{C}}_h(\omega) - \tilde{\mathbf{C}}_{ae}(V,\omega))\mathbf{G}_{\dot{\boldsymbol{\eta}}}(\omega) + (\tilde{\mathbf{K}}_s + \tilde{\mathbf{K}}_h - \tilde{\mathbf{K}}_{ae}(V,\omega))\mathbf{G}_{\boldsymbol{\eta}}(\omega) = \mathbf{G}_{\mathbf{Q}_{Buff}}(\omega) + \mathbf{G}_{\mathbf{Q}_{wave}}(\omega) \quad (1)$$

Here, $\mathbf{G}_{\boldsymbol{\eta}}$ is the Fourier transform of the displacement response; $\tilde{\mathbf{M}}_s$, $\tilde{\mathbf{C}}_s$ and $\tilde{\mathbf{K}}_s$ are the generalized mass, damping and stiffness matrices, respectively; $\tilde{\mathbf{C}}_{ae}$ and $\tilde{\mathbf{K}}_{ae}$ denote the generalized aerodynamic damping and stiffness matrices; $\tilde{\mathbf{M}}_h$ and $\tilde{\mathbf{C}}_h$ are the generalized hydrodynamic mass and damping matrices; $\tilde{\mathbf{K}}_h$ is the hydrostatic restoring fore; $\mathbf{G}_{\mathbf{Q}_{Buff}}$ is the Fourier transform of the wind force on the girder; and $\mathbf{G}_{\mathbf{Q}_{wave}}$ is the Fourier transform of the first-order wave force on the pylons. The second-order wave forces are not considered in the paper since they are of minor importance for section forces in the cable-supported bridge with floating pylons [17].

The frequency domain approach mainly includes two steps: (1) the modal analysis of the structure, and (2) the modeling of the aerodynamic and hydrodynamic actions using generalized coordinates.

2.1.1 Structural modal analysis

The modal analysis is performed following a static analysis, wherein time-invariant mean wind forces are imposed upon the bridge. In addition, the added mass when the frequency goes to infinity and the hydrostatic restoring stiffness are added into the structural mass and stiffness matrices, respectively, since these effects will substantially alter the natural modes and frequencies. Consequently, fewer modes are required, and some computational time can be saved.

The deformation along the girder, pylons and pontoons for each natural mode must be applied for the calculations of the generalized wind and wave actions.

$$\begin{aligned}&\Phi(\mathbf{x}) = [\boldsymbol{\varphi}_1 \cdots \boldsymbol{\varphi}_i \cdots \boldsymbol{\varphi}_{N_{\text{mod}}}];\\ &\boldsymbol{\varphi}_i = [\varphi_y \quad \varphi_z \quad \varphi_{\theta x}]^T, \quad \textit{for girder}\\ &\boldsymbol{\varphi}_i = [\varphi_x \quad \varphi_y \quad \varphi_z \quad \varphi_{\theta x} \quad \varphi_{\theta y} \quad \varphi_{\theta z}]^T, \quad \textit{for pylons}\end{aligned} \tag{2}$$

where φ_n, $n \in \{x, y, z, \theta_x, \theta_y, \theta_z\}$ represents three translations and three rotations of the girder and pylons for each mode. The positive directions of the displacements along the girder, pylons, and pontoons are shown in Fig. 2 and 4. Not all the displacements are necessary for the girder since only the drag force, lift force and torsional moment along the girder are considered in this case study.

2.1.2 Wind actions in generalized coordinates

(1) Aerodynamic self-excited forces

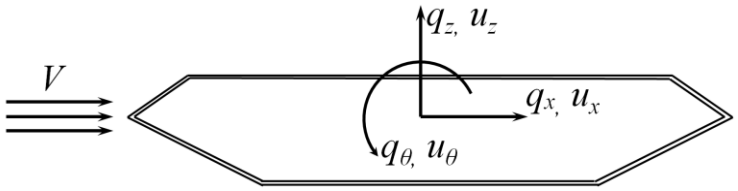

Fig. 2 Aerodynamic forces acting on a bridge deck cross-section

The self-excited forces acting on a bridge deck cross-section are commonly represented by the aerodynamic derivatives developed by Scanlan and Tomko [20]. The self-excited forces on a bridge deck for single-frequency harmonic motion can be expressed as follows:

$$\mathbf{q} = \mathbf{C}_{ae}(K)\dot{\mathbf{u}} + \mathbf{K}_{ae}(K)\mathbf{u} \tag{3}$$

The positive directions of the forces and moment are shown in Fig. 2. The displacements are positive in the same directions as the corresponding forces. The aerodynamic damping matrix $\mathbf{C}_{ae}$ and the aerodynamic stiffness matrix $\mathbf{K}_{ae}$ contain 18 aerodynamic derivatives, namely, P_n^*, H_n^* and A_n^*, $n \in \{1,2,...,6\}$, which represent functions of the reduced frequencies of motion with $K = (B\omega)/V$:

$$\mathbf{C}_{ae} = \frac{1}{2}\rho V K B \begin{bmatrix} P_1^* & P_5^* & BP_2^* \\ H_5^* & H_1^* & BH_2^* \\ BA_5^* & BA_1^* & B^2A_2^* \end{bmatrix}, \quad \mathbf{K}_{ae} = \frac{1}{2}\rho V^2 K^2 \begin{bmatrix} P_4^* & P_6^* & BP_3^* \\ H_6^* & H_4^* & BH_3^* \\ BA_6^* & BA_4^* & B^2A_3^* \end{bmatrix} \tag{4}$$

Here, V represents the mean wind velocity, ρ is the air density, and B is the width of the girder. The elements of the generalized aerodynamic stiffness and damping matrices $\tilde{\mathbf{C}}_{ae}$ and $\tilde{\mathbf{K}}_{ae}$ may then be calculated as follows [21]:

$$\begin{aligned}\tilde{C}_{nm}^{(\mathrm{ae})}(V,\omega) &= \int_{girder} \boldsymbol{\varphi}_n^T \mathbf{C}_{ae}(V,\omega)\boldsymbol{\varphi}_m dx \\ \tilde{K}_{nm}^{(\mathrm{ae})}(V,\omega) &= \int_{girder} \boldsymbol{\varphi}_n^T \mathbf{K}_{ae}(V,\omega)\boldsymbol{\varphi}_m dx\end{aligned} \tag{5}$$

(2) Buffeting forces on the girder

The density of the air is assumed to be $\rho = 1.25$ kg/m^3, and the cross-spectral densities of the horizontal along-wind velocity component u and vertical velocity component w at the points i and j are assumed as follows:

$$\begin{aligned}S_{uu}^{+}(\omega,\Delta x) &= \frac{40.58Vz\kappa}{(1+9.74\omega z/V)^{5/3}}\exp(-\frac{2.8\omega\Delta x}{V}) \\ S_{ww}^{+}(\omega,\Delta x) &= \frac{0.82Vz\kappa}{(1+0.79\omega z/V)^{5/3}}\exp(-\frac{\Delta x\omega}{V}) \\ S_{uw}^{+}(\omega,\Delta x) &= \frac{2.23Vz\kappa}{(1+1.67\omega z/V)^{7/3}}\exp(-\frac{\Delta x\omega}{V})\end{aligned} \tag{6}$$

Here, κ is the roughness coefficient at the site, assumed to be 0.0031; and Δx is the distance between the two points considered. The vertical curvature of the girder is neglected by using the height at the middle of the bridge as reference for the wind load of the girder.

The elements in the cross spectral density matrix of the generalized wind actions can be written as follows:

$$\tilde{S}_{\mathbf{Q}_{buff_{nm}}} = \iint \boldsymbol{\varphi}_n^T(x_1)\mathbf{B}_q\mathbf{S}_v^{+}\mathbf{B}_q^T\boldsymbol{\varphi}_m(x_2)dx_1dx_2 \tag{7}$$

$$\mathbf{B}_q = \frac{\rho VB}{2}\begin{bmatrix} 2(D/B)\bar{C}_D & (D/B)C_D' - C_L' \\ 2\bar{C}_L & C_L' + (D/B)\bar{C}_D \\ 2B\bar{C}_M & BC_M' \end{bmatrix},\quad \mathbf{S}_v^{+} = \begin{bmatrix} S_{uu}^{+} & S_{wu}^{+} \\ S_{uw}^{+} & S_{ww}^{+} \end{bmatrix}$$

Here, $\mathbf{B}_q$ is the wind force transfer function. D denotes the height of the girder. $\bar{C}_D$, $\bar{C}_L$ and $\bar{C}_M$ are the mean values of the drag, lift and torsional moment force coefficients on the girder; and C_D', C_L' and C_M' are their derivatives with respect to the angle of attack.

2.1.3 Wave actions in a generalized coordinate system

(1) Radiation force

When a floating structure oscillates from the effects of waves or within still water, it will generate outgoing waves, thereby resulting in oscillating fluid pressures on the body surface [22]. The integrated hydrodynamic pressures are identified as the radiation force, which consists of the added mass $\mathbf{M}_h$ and the damping $\mathbf{C}_h$:

$$\mathbf{F}_{se}^{(\mathrm{H})} = \mathbf{M}_h(\omega)\ddot{\mathbf{u}} + \mathbf{C}_h(\omega)\dot{\mathbf{u}} \tag{8}$$

When the oscillation frequency ω goes to infinity, the damping converges to zero while the added mass becomes constant and frequency independent.

$$\begin{aligned} \mathbf{M}_h(\omega) &= \mathbf{m}_h(\omega) + \mathbf{M}_h(\infty) \\ \mathbf{C}_h(\omega) &= \mathbf{c}_h(\omega) + \mathbf{C}_h(\infty) = \mathbf{c}_h(\omega) \end{aligned} \tag{9}$$

$\mathbf{M}_h(\infty)$ is added into the structural mass matrix as discussed in section 2.1.1. Upon considering the frequency-dependent part only, the elements of the generalized hydrodynamic added mass and damping matrices can be calculated as follows:

$$\begin{aligned} \tilde{\mathbf{M}}_{nm}^{(h)} &= \sum_{i=1}^{2} \boldsymbol{\varphi}_n^T(x_i)\mathbf{m}_h\boldsymbol{\varphi}_m(x_i) \\ \tilde{\mathbf{C}}_{nm}^{(h)} &= \sum_{i=1}^{2} \boldsymbol{\varphi}_n^T(x_i)\mathbf{c}_h\boldsymbol{\varphi}_m(x_i) \end{aligned} \tag{10}$$

Here, $i \in \{1,2\}$ refers to the two pylons.

(2) First-order wave excitation forces

The irregular short-crested wave spectrum is a function of both the frequency and the wave direction:

$$S_\eta(\omega,\theta) = S(\omega)D(\omega,\theta) \tag{11}$$

Here $S(\omega)$ is the unidirectional wave spectral density and $D(\omega,\theta)$ the directional distribution. The directional function for locally generated sea states is commonly approximated as frequency independent. The Jonswap spectrum is then used to estimate the unidirectional wave spectral density and the cos-2s distribution [23] for directional spreading:

$$S(\omega) = (1-0.287\ln(\gamma))\frac{5H_s^2\omega_p^4}{16\omega^5}\exp\left(-\frac{5}{4}\left(\frac{\omega_p}{\omega}\right)^4\right)\gamma^{\exp\left(-0.5(\frac{\omega-\omega_p}{\sigma\omega_p})^2\right)}$$
$$D(\theta) = \frac{\Gamma(s+1)}{2\sqrt{\pi}\Gamma(s+1/2)}\cos^{2s}\left(\frac{\theta}{2}\right) \quad (12)$$

Here, H_s and ω_p denote the significant wave height and peak wave frequency, respectively; s is the wave directional parameter; γ is the non-dimensional peak shape parameter and is equal to 2.05 in this case study; and σ is the spectral width parameter:

$$\sigma = \begin{cases} 0.07 & \text{for } \omega \le \omega_p \\ 0.09 & \text{for } \omega > \omega_p \end{cases}$$

The auto- and cross-spectral densities of the first-order wave excitation force in each of the six directions can be written as follows:

$$\mathbf{S}_p = \int_\theta \mathbf{T}^{(1)} S_\eta \mathbf{T}^{(1)'} d\theta \quad (13)$$

The transfer function $\mathbf{T}^{(1)}(\omega,\theta)$ depends only upon the geometry of the floating structure; thus, $\mathbf{T}_1^{(1)}(\omega,\theta) = \mathbf{T}_2^{(1)}(\omega,\theta)$. Here, the subscripts 1 and 2 refer to the first and second pylons instead of the force components.

The elements in the generalized first-order wave action spectral matrix can be expressed as follows:

$$\tilde{S}_{p_{nm}} = \begin{bmatrix} \boldsymbol{\varphi}_n(\mathbf{x}_1) \\ \boldsymbol{\varphi}_n(\mathbf{x}_2) \end{bmatrix}^T \begin{bmatrix} \mathbf{S}_p & \mathbf{0} \\ \mathbf{0} & \mathbf{S}_p \end{bmatrix} \begin{bmatrix} \boldsymbol{\varphi}_m(\mathbf{x}_1) \\ \boldsymbol{\varphi}_m(\mathbf{x}_2) \end{bmatrix} \quad (14)$$

Here, $\mathbf{x}_1$ and $\mathbf{x}_2$ refer to the positions of the two pylons. The distance between the two pylons is approximately 1385 m, and thus, it is reasonable to ignore the cross-spectral densities of the wave force between them for short-crested waves.

2.1.4 Response in Cartesian coordinates

The total generalized system matrices are established by summing the contributions from the bridge with the girder-wind interactions and the pylon-water interactions. These matrices are then used to establish the generalized frequency domain transfer function $\tilde{\mathbf{H}}(\omega)$:

$$\tilde{\mathbf{H}}(\omega) = (-(\tilde{\mathbf{M}}_0 + \tilde{\mathbf{M}}_h)\omega^2 + (\tilde{\mathbf{C}}_0 + \tilde{\mathbf{C}}_h - \tilde{\mathbf{C}}_{ae})i\omega + (\tilde{\mathbf{K}}_0 - \tilde{\mathbf{K}}_{ae}))^{-1} \quad (15)$$

The spectral response matrix can be conveniently obtained via the transformation from a generalized into a Cartesian coordinate system:

$$\mathbf{S}_u(\omega,\mathbf{x}) = \boldsymbol{\varphi}(\mathbf{x})\left[\tilde{\mathbf{H}}(\omega)(\tilde{\mathbf{S}}_{buff} + \tilde{\mathbf{S}}_p + \tilde{\mathbf{S}}_p^{2\pm})\tilde{\mathbf{H}}(\omega)^T\right]\boldsymbol{\varphi}(\mathbf{x})^T \tag{16}$$

2.2 State-space time domain approach

The equation of motion in the time domain can be written as follows:

$$\mathbf{M}_s\ddot{\mathbf{u}}(\mathrm{t}) + \mathbf{C}_s\dot{\mathbf{u}}(t) + (\mathbf{K}_s + \mathbf{K}_h)\mathbf{u}(t) = \underbrace{\mathbf{F}_{mean} + \mathbf{F}_{Buff}(\mathrm{t}) + \mathbf{F}_{se}(\mathrm{t})}_{\mathbf{F}_{Aero}} + \underbrace{\mathbf{F}_{WA}^{(1)}(\mathrm{t}) - \mathbf{F}_{Rad}(\mathrm{t})}_{\mathbf{F}_{Hydro}} \tag{17}$$

Here, $\mathbf{M}_s$, $\mathbf{C}_s$ and $\mathbf{K}_s$ symbolize the still-air mass, damping and stiffness matrix, respectively, and $\mathbf{u}$ represents the degrees of freedom of the finite element model. $\mathbf{F}_{Aero}$ represents the wind actions, which consist of a time-invariant component $\mathbf{F}_{mean}$ due to the mean wind velocity, a dynamic component $\mathbf{F}_{Buff}$ due to turbulence in the wind field and self-excited forces $\mathbf{F}_{se}(\mathrm{t})$ generated by the motion of the girder. $\mathbf{F}_{Hydro}$ represents the wave actions, which consist of the radiation forces $\mathbf{F}_{Rad}$ induced by the motion of the submerged part of the pylons, the hydrostatic restoring stiffness $\mathbf{K}_h$, and the first-order wave excitation forces $\mathbf{F}_{WA}^{(1)}$.

2.2.1 Radiation forces in the time domain

By applying an inverse Fourier transform to Eq. (8), the radiation forces can be expressed in the time domain as follows:

$$\begin{cases} \mathbf{F}_{Rad}(\mathrm{t}) = \mathbf{z}_{Rad}(\mathrm{t}) + \mathbf{M}_h(\infty)\ddot{\mathbf{u}}(\mathrm{t}) \\ \mathbf{z}_{Rad}(\mathrm{t}) = \int_{-\infty}^{\infty}\mathbf{h}(\mathrm{t}-\tau)\dot{\mathbf{u}}(\tau)d\tau \end{cases} \tag{18}$$

Here, $\mathbf{h}(\mathrm{t})$ is the inverse Fourier transform of $\mathbf{H}(\omega)$ (i.e., $\mathbf{H}(\omega) = i\omega\mathbf{m}_h(\omega) + \mathbf{c}_h(\omega)$).

The relationship between the output (radiation force) and input (velocity) in Eq. (18) can be expressed as a state-space model that has previously been described in detail in [24]:

$$\begin{cases} \mathbf{z}_{Rad}(\mathrm{t}) = \left[z_1^{(Rad)}(\mathrm{t}) \;\; z_2^{(Rad)}(\mathrm{t}) \cdots z_6^{(Rad)}(\mathrm{t})\right]^T \\ z_i^{(Rad)}(\mathrm{t}) = \sum_{j=1}^{6} z_{ij}^{(Rad)}(\mathrm{t}) \\ \dot{\mathbf{X}}(\mathrm{t}) = \mathbf{D}_c^{(\mathrm{H})}\mathbf{X}(\mathrm{t}) + \mathbf{E}_c^{(\mathrm{H})}\dot{u}_j(\mathrm{t}) \\ z_{ij}^{(Rad)}(\mathrm{t}) = \mathbf{Q}_c^{(\mathrm{H})}\mathbf{X}(\mathrm{t}) \end{cases} \qquad i,j \in \{1,2,\cdots,6\} \tag{19}$$

where

$$\mathbf{X}(\mathrm{t})=\begin{bmatrix} X_1(\mathrm{t}) \\ X_2(\mathrm{t}) \\ \vdots \\ \vdots \\ \vdots \\ X_n(\mathrm{t}) \end{bmatrix}, \mathbf{D}_c^{(\mathrm{H})}=\begin{bmatrix} 0 & 0 & 0 & \cdots & 0 & -q_0 \\ 1 & 0 & 0 & \cdots & 0 & -q_1 \\ 0 & 1 & 0 & \cdots & 0 & -q_2 \\ \vdots & \vdots & \vdots & & \vdots & \vdots \\ 0 & 0 & 0 & \cdots & 0 & -q_{n-2} \\ 0 & 0 & 0 & \cdots & 1 & -q_{n-1} \end{bmatrix}, \mathbf{E}_c^{(\mathrm{H})}=\begin{bmatrix} p_0 \\ p_1 \\ p_2 \\ p_3 \\ \vdots \\ p_m \end{bmatrix}, \mathbf{Q}_c^{(\mathrm{H})}=\begin{bmatrix} 0 \\ 0 \\ 0 \\ 0 \\ \vdots \\ 1 \end{bmatrix}^T$$

Here, $z_{ij}^{(Rad)}$ is the radiation force in *i*th direction induced by the motion in *j*th direction. $\mathbf{X}$ is the state vector and updated at each time step. $\mathbf{D}_c^{(\mathrm{H})}$, $\mathbf{E}_c^{(\mathrm{H})}$ and $\mathbf{Q}_c^{(\mathrm{H})}$ are different among each of the 6×6 state-space models, and they can be determined through the least-square curve fitting of the transfer functions defined by the added mass and damping coefficients.

$$\hat{\theta}=\arg\min_{\theta}\sum_{l}\left|H_{ij}(\omega_l)-H_{ij}^{'}(i\omega_l,\theta)\right| \tag{20}$$

Here, $\theta=\left[p_m,\cdots,p_0,q_{n-1},\cdots,q_0\right]$ and $H_{ij}'(s,\theta)=\dfrac{p_m s^m+p_{m-1}s^{m-1}+\cdots+p_1 s+p_0}{s^n+q_{n-1}s^{n-1}+\cdots+q_1 s+q_0}$, and l is the number of sampling points.

2.2.2 Aerodynamic self-excited forces in the time domain

By applying an inverse Fourier transform to Eq. (3), the self-excited forces per unit length in the time domain can be expressed as a convolution integral as follows:

$$\mathbf{q}(\mathrm{t})=\int_{-\infty}^{\infty}\mathbf{f}(\mathrm{t}-\tau)\mathbf{u}(\tau)d\tau$$

Similar to modeling the radiation forces, the transfer function presented above can be expressed as a state-space model [25-28]. After integrating the distributed self-excited forces by applying the principle of virtual work and then introducing the state-space model yields the following expression for the nodal forces [28, 29]:

$$\begin{cases} \mathbf{F}_{se}=\mathbf{A}_1\mathbf{u}(\mathrm{t})+\mathbf{A}_2\dot{\mathbf{u}}(\mathrm{t})+\mathbf{z}_{se}(\mathrm{t}) \\ \dot{\mathbf{X}}(\mathrm{t})=\mathbf{D}_c^{(ae)}\mathbf{X}(\mathrm{t})+\mathbf{E}_c^{(ae)}\dot{\mathbf{u}}(\mathrm{t}) \\ \mathbf{z}_{se}(\mathrm{t})=\mathbf{Q}_c^{(ae)}\mathbf{X}(\mathrm{t}) \end{cases} \tag{21}$$

where

$$\mathbf{A}_1 = \frac{1}{2}\rho V^2 \int_0^L \mathbf{N}^T(y)\mathbf{a}_1\mathbf{N}(y)dy; \qquad \mathbf{A}_2 = \frac{1}{2}\rho V^2 \frac{B}{V}\int_0^L \mathbf{N}^T(y)\mathbf{a}_2\mathbf{N}(y)dy;$$

$$\mathbf{D}_c^{(ae)} = \frac{V}{B}\begin{bmatrix} d_1\mathbf{I} & & & \\ & d_1\mathbf{I} & & \\ & & \ddots & \\ & & & d_{N-3}\mathbf{I} \end{bmatrix}; \qquad \begin{aligned} \mathbf{E}_c^{(ae)} &= [\mathbf{I} \quad \mathbf{I} \quad \cdots \quad \mathbf{I}]^T; \\ \mathbf{Q}_c^{(ae)} &= [\mathbf{A}_4 \ \mathbf{A}_5 \cdots \mathbf{A}_N]; \\ \mathbf{X} &= [\mathbf{x}_1 \ \mathbf{x}_2 \cdots \mathbf{x}_{N-3}]^T \end{aligned} .$$

Here, $\mathbf{I}$ is the identity matrix; $\mathbf{A}_{l+3} = \frac{1}{2}\rho V^2 \int_0^L \mathbf{N}^T(y)\mathbf{a}_{l+3}\mathbf{N}(y)dy$; and $\mathbf{x}_l = \mathbf{u}(\mathrm{t}) - \frac{d_l V}{B}\int_{-\infty}^{t} e^{-(d_l V/B)(\mathrm{t}-\tau)}\mathbf{u}(\tau)\,\mathrm{d}\tau$.

The matrix $\mathbf{N}(y)$ includes the shape functions, and L refers to the length of the beam element.

$$\mathbf{F}(\omega) = \frac{1}{2}\rho V^2 (\mathbf{a}_1 + \mathbf{a}_2 \frac{i\omega B}{V} + \sum_{l=1}^{N-3} \mathbf{a}_{l+3} \frac{i\omega B/V}{i\omega B/V + d_l}) \tag{22}$$

The unknowns $\mathbf{a}_1$, $\mathbf{a}_2$, $\mathbf{a}_{l+3}$ and the value of d_l in the rational function can be obtained through the least-square curve fitting of the experimental data of the aerodynamic derivatives.

2.2.3 Wind and wave excitation forces

The mean and buffeting forces attributable to the mean and turbulent wind actions, respectively, are calculated using the quasi-steady theory [30] when the aerodynamic admittance is neglected. Assuming that the fluctuating flow components $u(x,t)$ and $w(x,t)$ and the structural velocity are small relative to the mean wind velocity V, the linearized wind-induced forces can be defined as follows:

$$\mathbf{F}_{mean} + \mathbf{F}_{Buff}(\mathrm{t}) = \frac{\rho V^2 B}{2}\begin{bmatrix} (D/B)\bar{C}_D \\ \bar{C}_L \\ B\bar{C}_M \end{bmatrix} + \frac{\rho V B}{2}\begin{bmatrix} 2(D/B)\bar{C}_D & (D/B)C'_D - C'_L \\ 2\bar{C}_L & C'_L + (D/B)\bar{C}_D \\ 2B\bar{C}_M & BC'_M \end{bmatrix}\begin{bmatrix} u(x,t) \\ w(x,t) \end{bmatrix} \tag{23}$$

At the peaks of the turbulent wind velocities, the higher-order terms can significantly contribute to the wind loading and thus to the load effects in certain situations. The buffeting forces are modeled using the following expression to investigate the influences of nonlinear terms:

$$\begin{aligned} \mathbf{F}_{mean} + \mathbf{F}_{Buff}(\mathrm{t}) &= \frac{1}{2}\rho V_{rel}^2 \begin{bmatrix} \cos\beta & -\sin\beta & 0 \\ \sin\beta & \cos\beta & 0 \\ 0 & 0 & 1 \end{bmatrix}\begin{bmatrix} D(\bar{C}_D + \beta C'_D) \\ B(\bar{C}_L + \beta C'_L) \\ B^2(\bar{C}_M + \beta C'_M) \end{bmatrix} \\ V_{rel}^2 &= (V + u(x,\mathrm{t}))^2 + w(x,\mathrm{t})^2 \\ \beta &\approx \arctan(\frac{w(x,\mathrm{t})}{V + u(x,\mathrm{t})}) \end{aligned} \tag{24}$$

For irregular waves, the first-order forces can be obtained by summing the contributions from all of the frequency components in all of the directions using the following well-known expression [31]:

$$\mathbf{F}_{WA}^{(1)}(x,y,t)=\sum_{n}^{N}\sum_{m}^{M}\left|\mathbf{T}^{(1)}(\omega_n,\theta_m)\right|\eta_{nm}\cos\left[k_n(x\cos(\theta_m)+y\sin(\theta_m))-\omega_n t+\varepsilon_{mn}-\phi_{mn}\right],\qquad i\in\{1,2,\cdots,6\}$$
$$\eta_{nm}=\sqrt{2S_\eta(\omega_n,\theta_m)\Delta\omega\Delta\theta} \tag{25}$$
$$\phi_{mn}=\tan^{-1}\left(\frac{\mathrm{Im}(\mathbf{T}^{(1)}(\omega_n,\theta_m))}{\mathrm{Re}(\mathbf{T}^{(1)}(\omega_n,\theta_m))}\right)$$

Here, k is the wave number and $\varepsilon_{mn}\in\{0\ldots 2\pi\}$ is a uniformly distributed random phase angle.

3. Long-term extreme value prediction methods

The FLM, ECM and IFORM are three of the most popular methods that are utilized to determine the characteristic values of long-term extreme load effects on offshore structures due to wind and wave action. However, as the ECM and IFORM are approximate approaches, their accuracies must be verified via the FLM.

3.1 Full long-term method and simplified FLM

In principle, the FLM approach is the most accurate for determining extreme load effects for design checks. The cumulative distribution function (CDF) of the extreme value $\hat{X}=\hat{X}(T)$, that is, the extreme value over a long-term period T, can be expressed as the integral of the short-term response over all possible environmental conditions [3]:

$$F_{\hat{X}}(\zeta)=\exp\left\{-T\int_V\int_{H_s}\int_{T_p}\nu_X^+(\zeta\,|v,h_s,t_p)\,f(v,h_s,t_p)\,dv\,dh_s\,dt_p\right\} \tag{26}$$

Here, ν_X^+ denotes the average ζ-upcrossing rate for a short-term environmental condition. For a zero-mean, stationary Gaussian process, ν_X^+ can be written as follows:

$$\nu_X^+(\zeta)=\frac{\sigma_{\dot{X}}(v,h_s,t_p)}{2\pi\sigma_X(v,h_s,t_p)}\exp\left(-\frac{\zeta^2}{2\sigma_X(v,h_s,t_p)^2}\right) \tag{27}$$

where the standard deviations σ_X and $\sigma_{\dot{X}}$ for long-term situations are functions of the environmental conditions. Substituting Eq. (27) into Eq. (26), the long-term extreme value distribution can be expressed as follows:

$$F_{\hat{X}}(\zeta)=\exp\left\{-T\int_V\int_{H_s}\int_{T_p}\frac{\sigma_{\dot{X}}(v,h_s,t_p)}{2\pi\sigma_X(v,h_s,t_p)}\exp(-\frac{\zeta^2}{2\sigma_X(v,h_s,t_p)^2})f(v,h_s,t_p)dvdh_sdt_p\right\} \quad (28)$$

As mentioned earlier, not all the conditions contribute to the extreme value distribution. In the simplified FLM, only the environmental conditions that yield significant contributions are accounted for. By determining an appropriate range of parameters, the computational times can be significantly reduced. The contribution from each environmental condition to the extreme value distribution of the load effects is dependent on $\nu_X^+(\zeta|v,h_s,t_p)f(v,h_s,t_p)$, which is the product of the conditional short-term extreme values and the probability density function of the corresponding environmental condition.

3.2 Inverse first-order reliability method

Unfortunately, since the FLM must account for the contributions from all possible short-term states, it is not the most economical method from a computational perspective. The IFORM is a relatively efficient approach that is utilized to achieve the extreme response corresponding to a given exceedance probability. A limit state function is defined as follows:

$$g(X_d,V,H_s,T_p;X_{\text{crit}})=X_{\text{crit}}-X_d(V,H_s,T_p) \quad (29)$$

Here X_d, which is a random variable, is the short-term extreme value. Failure refers to an event when the critical response X_{crit} is exceeded by X_d, and thus, the failure probability can be approximated as follows [3]:

$$p_f(X_{\text{crit}})=1-F_{\hat{X}}(X_{\text{crit}})=\underset{g(X_d,V,H_s,T_p;X_{\text{crit}})<0}{\int\int\int\int}f_{X_d|V,H_s,T_p}(\zeta|v,h_s,t_p)f(v,h_s,t_p)dvdh_sdt_pd\zeta \quad (30)$$

Here, three environmental parameters are considered: the mean wind velocity *V*, the significant wave height H_s and the peak wave period T_p. For complex structures experiencing both wind and waves, other important parameters, e.g., the wind velocity, turbulence intensity and the wind and wave directions, must also be considered and will consequently be studied in future investigations. Directly solving Eq. (30) is not efficient, and therefore, this integral is transformed to a U-space consisting of independent, standard Gaussian variables (u_1,u_2,u_3,u_4). This can be accomplished by for instance using the so-called Rosenblatt transformation scheme [32].

$$
\begin{aligned}
F_V(v) = \Phi(u_1) \quad &\Leftrightarrow \quad u_1 = \Phi^{-1}\left[F_V(v)\right] \\
F_{H_s|V}(h_s|v) = \Phi(u_2) \quad &\Leftrightarrow \quad u_2 = \Phi^{-1}\left[F_{H_s|V}(h_s|v)\right] \\
F_{T_P|V,H_s}(t_p|v,h_s) = \Phi(u_3) \quad &\Leftrightarrow \quad u_3 = \Phi^{-1}\left[F_{T_P|V,H_s}(t_p|v,h_s)\right] \\
F_{X_d|H_s,V,T_P}(x|h_s,v,t_p) = \Phi(u_4) \quad &\Leftrightarrow \quad u_4 = \Phi^{-1}\left[F_{X_d|H_s,V,T_P}(x|h_s,v,t_p)\right]
\end{aligned}
\tag{31}
$$

After transformation, the failure probability can be expressed as follows:

$$
p_f(X_{\text{crit}}) = \int\int\int\int\int_{g(X_d,V,H_s,T_p;X_{\text{crit}})<0} \phi_{\text{U}}(\mathbf{u})d\mathbf{u} \tag{32}
$$

where ϕ_{U} is the joint probability density function for the Gaussian variables.

The IFORM assumes that the limit state function $g(\mathbf{u}; X_{\text{crit}}) = 0$ in the U-space can be approximated linearly via a first-order Taylor expansion. Prior to this assumption, there is no loss of accuracy. Furthermore, to guarantee that the first-order approximation will introduce the least error, the limit state function is expanded at the most probable point (MPP), which provides the greatest contribution to the failure probability. In the U-space, the MPP is the point on the limit state surface with the minimal distance, β, from the origin. The failure probability under the assumption of first-order expansion can be written as follows [33]:

$$
p_f = \Phi(-\beta)
$$

As the annual probability of exceedance is given, a hypersphere with a radius β can be determined. The purpose of the IFORM is to find the design point that yields the largest response on the hypersphere.

Given, p_f;

find, $X_{\text{crit}} = \max(X_d(\mathbf{u}))$ subject to $|\mathbf{u}| = \beta$ where $\beta = -\Phi^{-1}(p_f)$

To perform the IFORM based on combined frequency domain and time domain simulation results, the U-space is divided into frequency domain region and time domain region, as shown in Fig. 3. During each iteration, it should firstly be determined in which region the condition $\mathbf{u}^k$ is located and then the following recursive formula can be used to achieve the design point [2]:

$$
\mathbf{u}^{k+1} = -\beta \frac{\nabla(\mathrm{g}(\mathbf{u}^k))}{\left|\nabla(\mathrm{g}(\mathbf{u}^k))\right|} \tag{33}
$$

Here, the notation ∇ is used for the gradient. The design point is obtained as $\left|\mathbf{u}^{k+1}-\mathbf{u}^{k}\right|/\left|\mathbf{u}^{k+1}\right| \le \varepsilon$, where ε is the convergence tolerance. A back-tracking approach [34, 35] is applied to modify the updated condition $\mathbf{u}^{k+1}$ in order to avoid the iteration conditions oscillating among several conditions without convergence because $\mathbf{u}^{k+1}$ calculated from Eq. (33) is not guaranteed to give a sufficient decrease of limit state function. See [34, 35] for further details.

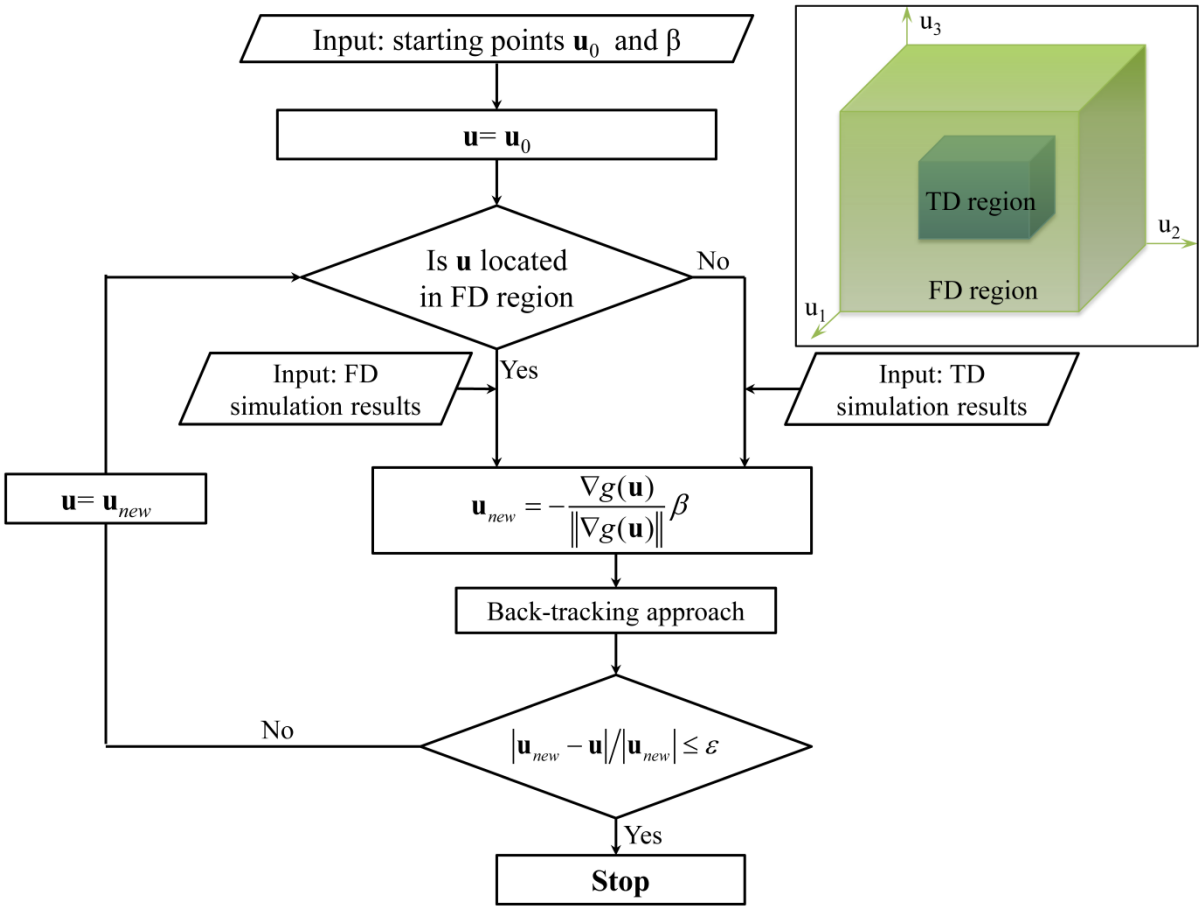

Fig. 3 Algorithm of the IFORM based on the combined frequency domain and time domain simulation results. FD and TD represent frequency domain and time domain, respectively.

3.3 Environmental contour method

If it is assumed that the conditional probability density function of the short-term extreme value in Eq. (30) approaches a Dirac delta function, then the random variable X_d can be replaced with its median value $X_d^{50\%}$, which is a deterministic value, and the integral over ζ can be removed [14] as follows:

$$p_f(X_{crit}) = 1 - F_{\hat{X}}(X_{crit}) = \iiint\limits_{g(X_d^{50\%}(V,H_s,T_p);X_{crit})<0} f(v,h_s,t_p)\,dv\,dh_s\,dt_p \tag{34}$$

This assumption represents the fundamental principle of ECM, which is clearly a simplification of the IFORM. Here, the probability of exceeding a given response level is independent of the response quantity and can be estimated simply from the joint distribution of the environmental conditions. Similar to Eq. (32), the failure probability above can be rewritten in standard Gaussian space as follows:

$$p_f(\zeta_{crit}) = 1 - F_{\hat{X}}(\zeta_{crit}) = \iiint_{g(X_d^{50\%}(\mathbf{u});X_{\text{crit}})<0} f_{\mathbf{U}}(\mathbf{u})d\mathbf{u} \tag{35}$$

The q-annual probability contour surface can be determined in the U-space by applying the IFORM. The only difference in this process is that the coordinate representing the variability in the short-term extreme response u_4 is assumed to be zero. By identifying the largest median response along the obtained contour surface, an estimate of the long-term extreme value distribution can be obtained.

When a random variable is replaced with a deterministic value, the corresponding long-term response will be non-conservative. Various approaches can be employed to compensate for the omitted variability in the response [10]. For instance, a higher percentile is selected as the short-term characteristic rather than selecting a median extreme response. Using a correction factor is another approach to compensate for the inaccuracies introduced by disregarding the uncertainty of the short-term extreme responses. The factor is structure-dependent. Studies have shown that it is in the range from 1.1 to 1.3 when calculating the load effects corresponding to an annual exceedance probability of 10^{-2} for offshore structures [1, 14, 36]. It is however important to be aware of that either selecting a higher percentile or using a correction factor is an approximation. The basic principle of the ECM is as follows:

Given, p_f;

find, $X_{crit} = \max(X_d^p(\mathbf{u}))$, where p is a constant larger than 50%;

or find, $X_{crit} = (1.1 \sim 1.3) \times \max(X_d^{50\%}(\mathbf{u}))$, subject to $|\mathbf{u}| = -\Phi^{-1}(p_f)$

In a weakly nonlinear dynamic problem, it is reasonable to assume that the most important condition on the environmental contour surface and the correction factor are the same. To avoid tremendous time domain simulations, the most important condition and the correction factor can be determined

based on frequency domain simulation results. Thus, only the most important condition will be simulated in time domain by considering the nonlinear properties.

4. Numerical results

A comprehensive finite element model of the bridge (displayed in Fig. 4) is used for the dynamic analysis (see [37] for details of the bridge model). Each span of the bridge has a length of 1385 m and the floating pylons are approximately 200 m above the mean water level and have a draft of 65 m. The girder, main cable, tethers, hangers and pylons are modelled using the beam elements in ABAQUS [38]. The geometry of the submerged part of the pylon in WADAM program (Wave Analysis by Diffraction and Morison Theory) [39] is modelled in an identical manner to the actual one instead of being simplified to a beam. The user elements, developed as a one-node element in the nodes of the girder and the gravity center of the submerged part of the floating pylons as illustrated by the red markers in the figure, are used in time-domain analysis to simulated the aerodynamic self-excited forces and radiation forces which are represented by state space model.

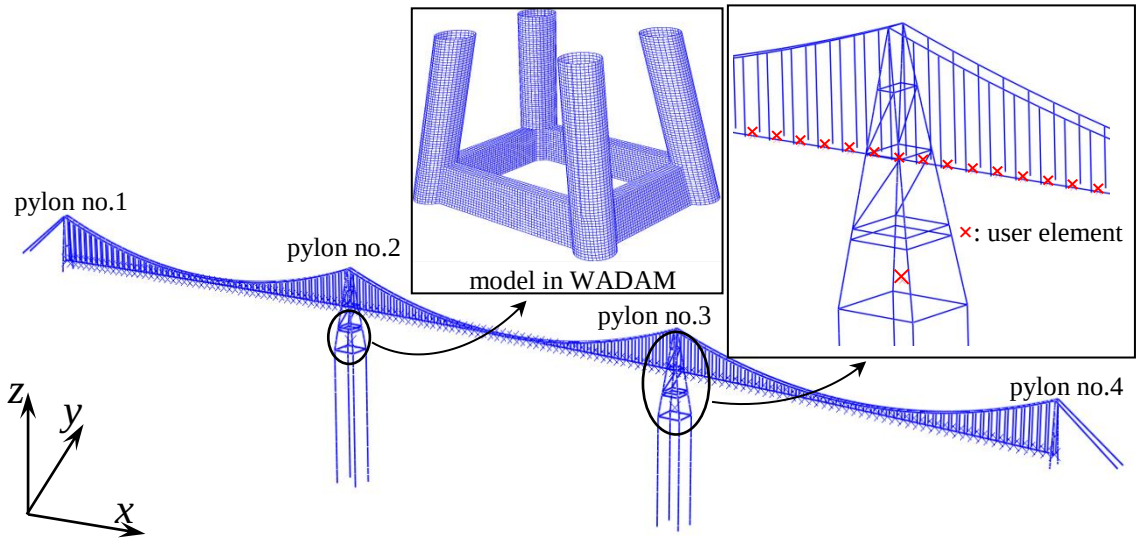

Fig. 4 Finite element model of the three span suspension bridge with two floating pylons

4.1 Long-term descriptions of the wind and wave conditions

Since measurements of the environmental conditions in Bjørnafjorden are currently not available, a scaled dataset from the North Sea is used in this paper, wherein the wave height and period are divided

by 2.5 and $\sqrt{2.5}$, respectively. The marginal distribution of V and the conditional distribution of H_s given the mean wind velocity are presented using a

model. Meanwhile, the conditional distribution of T_p given both the mean wind velocity and the significant wave height is fitted to a lognormal distribution. Table 1 lists the assumed parameters [40, 41].

$$f_V(v) = \frac{\alpha_V}{\beta_V}\left(\frac{v}{\beta_V}\right)^{\alpha_V - 1} \cdot \exp\left(-\left(\frac{v}{\beta_V}\right)^{\alpha_V}\right) \tag{36}$$

$$f_{H_s|V}(h_s|v) = \frac{\alpha_{Hs}}{\beta_{Hs}}\left(\frac{h_s}{\beta_{Hs}}\right)^{\alpha_V - 1} \cdot \exp\left(-\left(\frac{h_s}{\beta_{Hs}}\right)^{\alpha_{Hs}}\right) \tag{37}$$

$$\alpha_{Hs} = a_1 + a_2 \cdot v^{a_3}; \quad \beta_{Hs} = b_1 + b_2 \cdot v^{b_3}$$

$$f_{T_p|V,H_s}(t_p|v,h_s) = \frac{1}{\sqrt{2\pi}\sigma_{\ln(T_p)} t_p} \cdot \exp\left[-\frac{1}{2}\left(\frac{\ln(t_p) - \mu_{\ln(T_p)}}{\sigma_{\ln(T_p)}}\right)^2\right] \tag{38}$$

$$\mu_{\ln(T_p)} = \ln\left(\frac{\mu_{T_p}}{\sqrt{1+\upsilon_{T_p}^2}}\right), \quad \sigma^2_{\ln(T_p)} = \ln(1+\upsilon^2_{T_p}), \quad \upsilon_{T_p} = \frac{\sigma_{T_p}}{\mu_{T_p}}$$

$$\mu_{T_p} = (e_1 + e_2 \cdot h_s^{e_3}) \cdot \left[1 + \theta\left(\frac{v - (f_1 + f_2 \cdot h_s^{f_3})}{f_1 + f_2 \cdot h_s^{f_3}}\right)^{\gamma}\right]; \quad \upsilon_{T_p} = k_1 + k_2 \cdot \exp(k_3 h_s)$$

Table 1 Parameters for the marginal distribution of V and the conditional distributions of H_s and T_p

α_V	β_V	θ	γ	a_1	a_2	a_3	b_1	b_2	b_3
2.209	9.409	-0.255	1.0	2.136	0.013	1.709	1.816	0.024	1.787
e_1	e_2	e_3	f_1	f_2	f_3	k_1	k_2	k_3	
8.0	1.938	0.486	2.5	3.001	0.745	-0.001	0.316	-0.145	

4.2 Wind- and wave-induced responses

The variations in the response of the floating suspension bridge under various combinations of wind velocity, wave height and peak period are shown in Fig. 5. At a specified wave period, the wave excitation force, wind buffeting force and aerodynamic damping represent the three primary parameters that dominate the section moment in the girder. Sea states with greater significant wave height induce larger wave excitation forces and correspondingly larger section moments. However, the structural response is not always greater under the influence of stronger winds because the aerodynamic damping can also increase with the mean wind velocity. The trend depends on the ratio

of the contributions to the responses from wind and wave loads. Wind is the primary contributor at small wave heights, and the section moment increases with the wind velocity. In contrast, the section moment initially decreases at greater wave heights and then increases with increasing wind velocities. In addition, the variation in the section moments depends significantly on the wave period. The peaks in the bending moment due to vertical deformation are located within the wave period range from 3 s to 8 s, which contains several vertical natural modes.

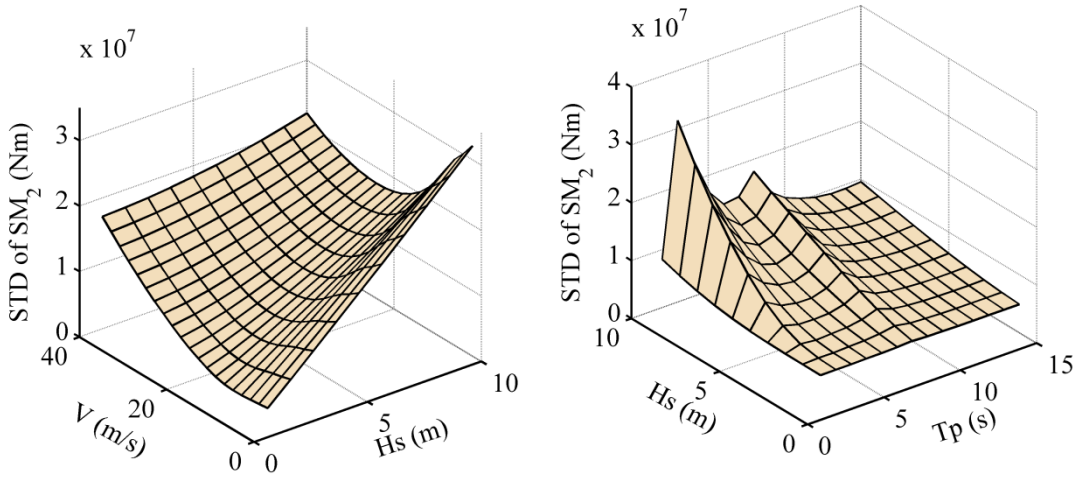

(a) Tp=8 s *(b) V=20 m/s*

Fig. 5 Standard deviation (STD) of the bending moment due to vertical deformation

4.3 Comparison of short-term extreme values obtained using the time and frequency domain methods

Both the multi-mode frequency domain method and the state-space time domain method can be employed to numerically simulate the response of a bridge within a linearized system. Meanwhile, the dynamic behavior of a bridge is normally simulated in the time domain for a nonlinear system in consideration of the geometric nonlinearity and nonlinear buffeting forces.

Time series of the stochastic horizontal and vertical wind velocity components along the bridge at V=30.7 m/s and the wave elevation for H_s=4.8 m and T_p=8 s are generated through Monte Carlo simulations (Figs. 6 through 8). The average co-spectral density of the 10 generated turbulent wind velocity realizations at points with a separation of 110 m and the average auto-spectral density of the wave elevation at the position of pylon no.2 are also compared with the target spectral densities, the results of which indicate a good match.

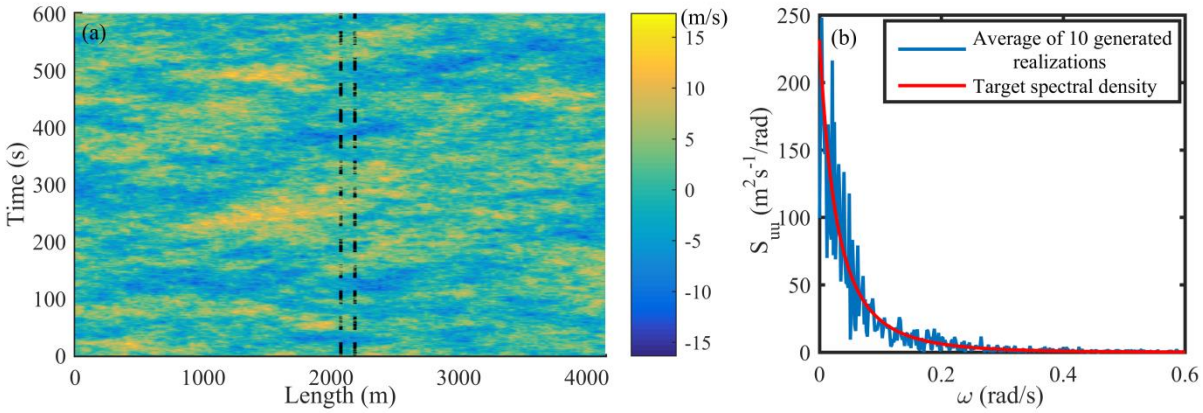

Fig. 6 (a) Time series of the horizontal wind component along the bridge at V=30.7 m/s. (b) Comparison of the average co-spectral density of the ten generated horizontal turbulent wind velocity realizations and the target co-spectral densities at two points with a separation of 110 m

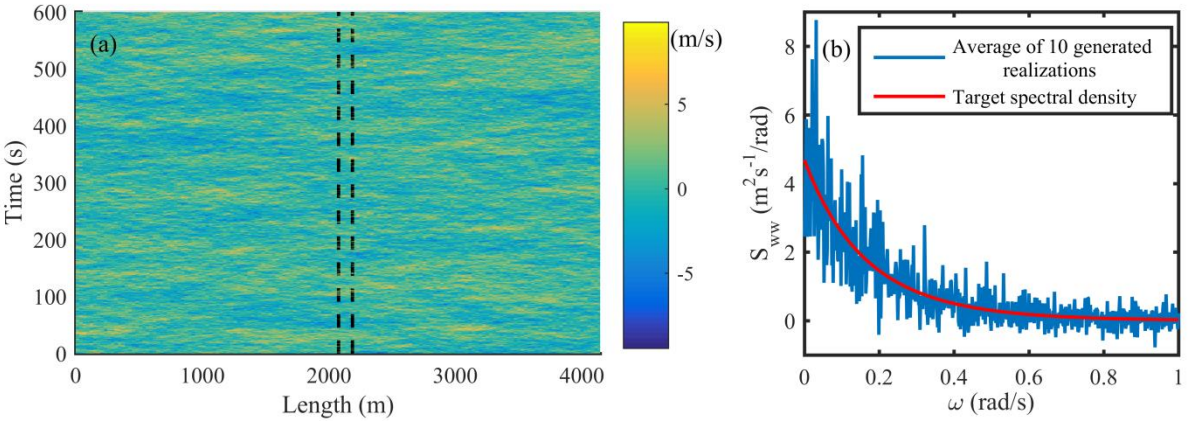

Fig. 7 (a) Time series of the vertical wind component along the bridge at V=30.7 m/s. (b) Comparison of the average co-spectral density of the ten generated vertical turbulent wind velocity realizations and the target co-spectral densities at two points with a separation of 110 m

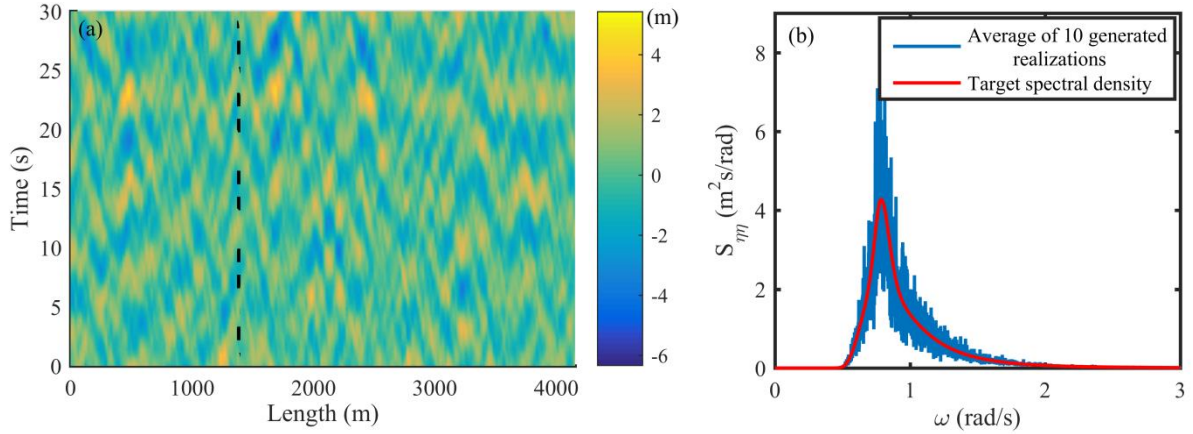

Fig. 8 (a) Time series of the wave elevations along the bridge at H_s=4.8 m and T_p=8 s. (b) Comparison of the average auto-spectral density of the ten simulated realizations and the target spectral densities at the position of pylon no.1.

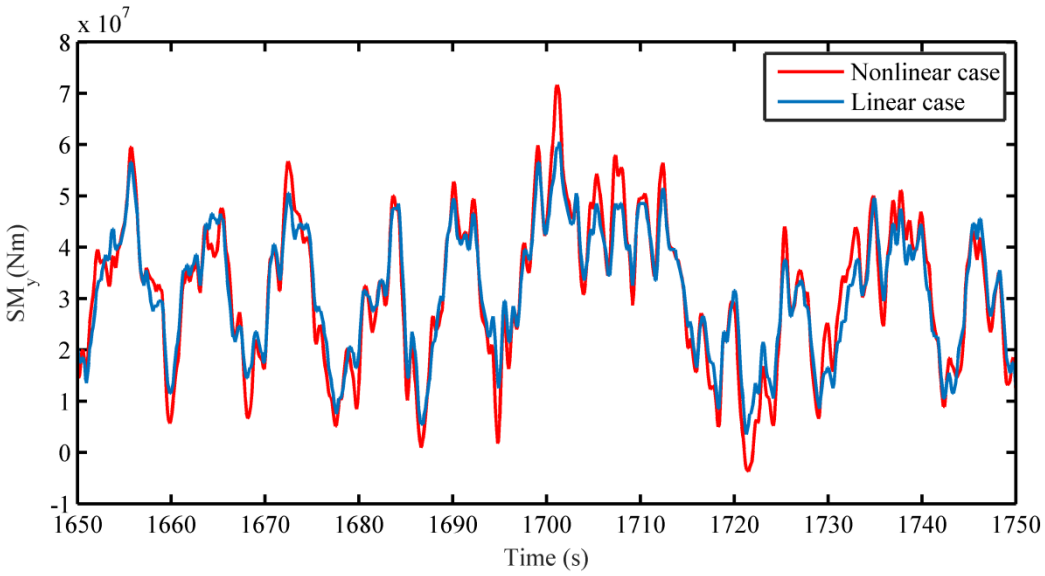

Fig. 9 Time series of the bending moment due to vertical deformation obtained from linear and nonlinear simulations

Fig. 9 displays the time series of the bending moment due to vertical deformation obtained using a linear and a nonlinear system. Some of the bending moment peaks from the nonlinear analysis are larger than those from the linear analysis. The average conditional exceedance rate (ACER) method [42] is used to process the time series history of the section force and calculate the short-term extreme value distribution:

$$F_X(\zeta) \approx \exp\left\{-\varepsilon_k(\zeta)\bar{N}T_{short}\right\} \tag{39}$$

where $\varepsilon_k(\zeta)$ denotes the average exceedance rates conditional on the k-1 previous non-exceedances of the threshold ζ, $\bar{N}$ is the average number of observed values per unit of time, and T_{short} is the period duration for a short-term case.

The mean exceedance rate $\varepsilon_k(\zeta)$ in the tail of a distribution is assumed to be dominated by a function of the form $q(\eta)\exp\left\{-e(\eta-b)^c\right\}(\eta \geq \eta_1 \geq \mathrm{b})$ [42], where η_1 is an appropriately chosen tail level. The four parameters e, b, c and q can be obtained via the curve fitting of the expression to the data obtained from the time series histories by utilizing the Levenberg-Marquardt least squares optimization method. Fig. 10(a) and (b) show satisfying curve fitting results for the 10 realizations of the section forces in one hour for both linear and nonlinear simulations using the ACER method.

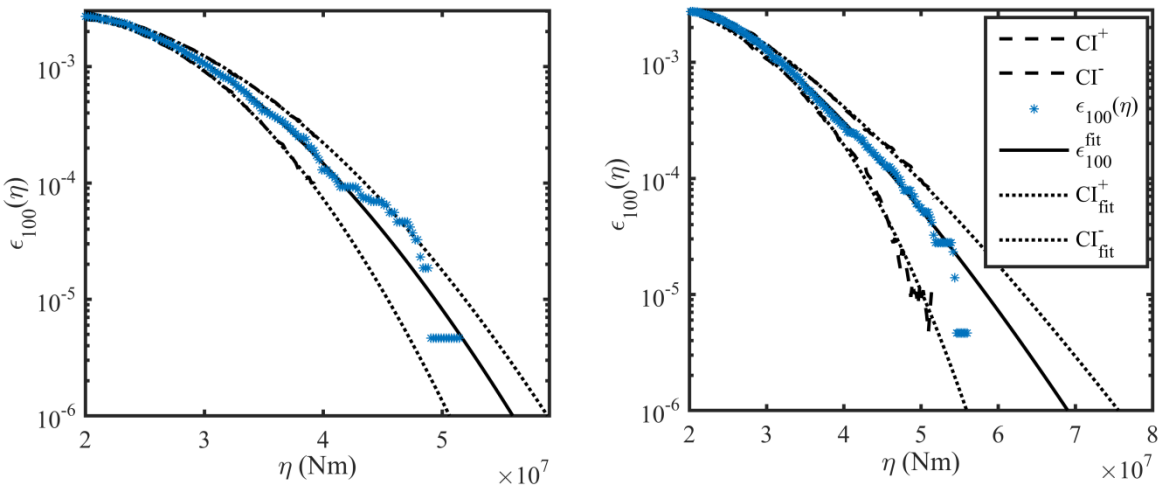

(a) ACER curve fitting results for the linear analysis

(b) ACER curve fitting results for the nonlinear analysis

Fig. 10 Average exceedance rates of the bending moment. $CI^{\pm}$ *and* $CI_{fit}^{\pm}$ *are the 95% confidence levels and their corresponding curve fitting results, respectively*

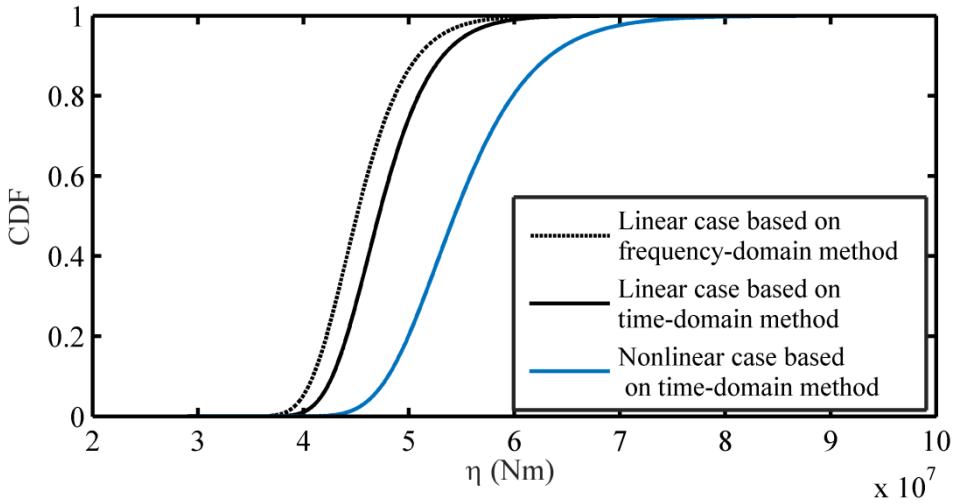

Fig. 11 Comparison of the short-term extreme value distributions obtained using the linear and nonlinear methods

The short-term extreme value distribution can also be calculated based on the frequency domain results as follows:

$$F_X(\zeta) = \exp\left\{-T\frac{\sigma_{\dot{X}}(V,H_s)}{2\pi\sigma_X(V,H_s)}\exp\left(-\frac{\zeta^2}{2\sigma_X(V,H_s)^2}\right)\right\} \tag{40}$$

Fig. 11 shows a comparison of the short-term extreme values obtained using the frequency domain method and the linear and nonlinear time domain methods. The 'linear time domain method' refers to the approach that does not consider nonlinear effects in the time domain simulations. It is only employed in the comparison with the frequency-domain results in this section to verify that the time-

and frequency-domain results corresponds for the linear system. The nonlinear effects are included in the time-domain analysis when performing the ECM and IFORM. Only very small differences exist between the linear time domain results and the frequency domain results; these differences were probably induced by the variability in the generated stochastic wind and wave fields or from the curve fitting of the mean exceedance rate. The comparison between the results of the frequency domain analysis and those of the nonlinear analysis suggests that nonlinearities can constitute a difference of approximately 20% in the bending moment due to vertical deformation. This means that the frequency domain method can underestimate the extreme value significantly. However, the time domain approach is very time consuming in an FLM. Therefore, three efficient alternatives are introduced herein to analyze the long-term extreme values of the bending moment due to vertical deformation, i.e., the simplified FLM, the ECM and the IFORM.

4.4 Simplified full long-term method

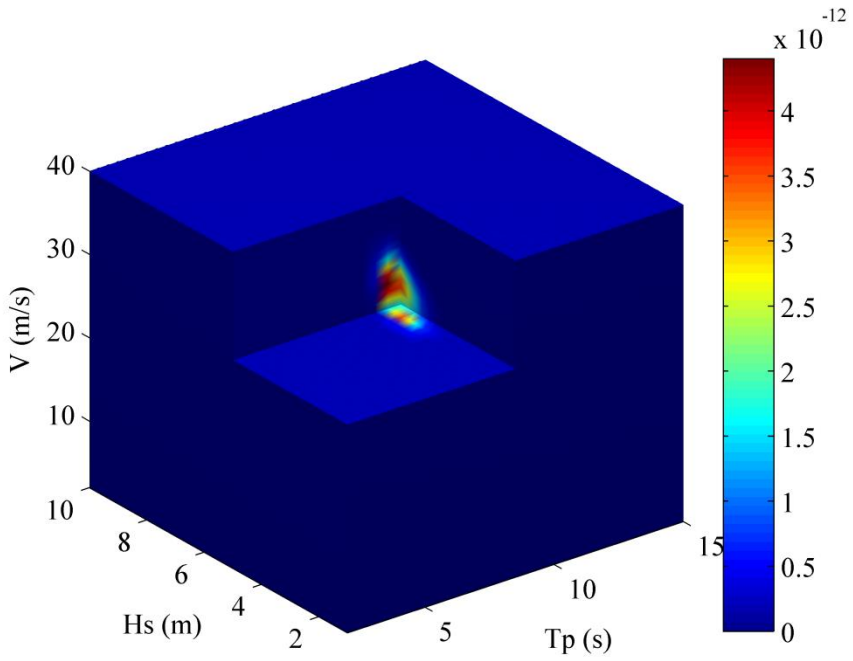

Fig. 12 Contribution from each environmental condition to the long-term extreme value distribution

Fig. 12 shows the contribution from each environmental condition to the long-term extreme value distribution. The results have been obtained applying the computationally efficient frequency-domain method. The colormap represents the product of the average ζ-upcrossing rate for a short-term

environmental condition and the probability density function of the corresponding environmental condition, $\nu_X^+(\zeta|v,h_s,t_p)f(v,h_s,t_p)$. The threshold ζ is selected to be equal to 50.43MNm. As shown in Fig. 12, only the wind velocities ranging from 25 to 35 m/s, the wave heights ranging from 3 to 7 m and the wave periods ranging from 7 to 10 s seem to yield significant contributions to the integration in Eq. (28). The long-term extreme value distribution for the bending moment, which is based on the FLM and the simplified FLM, is displayed in Fig. 13. The results in Fig. 13 confirm that only the environmental conditions in Table 2 contributed significantly to the long-term extreme values.

Therefore, the simplified FLM and FLM can predict equally accurate extreme values, and the former can save tremendous computational time. The simplified FLM based on the time-domain simulation results can be performed by assuming that the important region keeps the same when the nonlinear effects are included. It can also be performed by selecting an environmental condition inside of the important region determined based on the frequency-domain results and calculating its contribution to the long-term extreme load effects. The adjacent environmental conditions are then simulated and the corresponding contributions are added until the long-term extreme value converges. However, the number of environmental conditions required is still too large for practical purposes if the conditions are simulated in the time domain.

Table 2 List of environmental conditions that yielded significant contributions to the long-term extreme values based on frequency-domain results

Methods	V		Hs		Tp	
	Range	Interval	Range	Interval	Range	Interval
FLM	1 – 40 m/s	1 m/s	1 – 10 m	0.3 m	1 – 15 s	0.3 s
Simplified FLM	25 – 35 m/s	1 m/s	3 – 7 m	0.3 m	7– 10 s	0.3 s

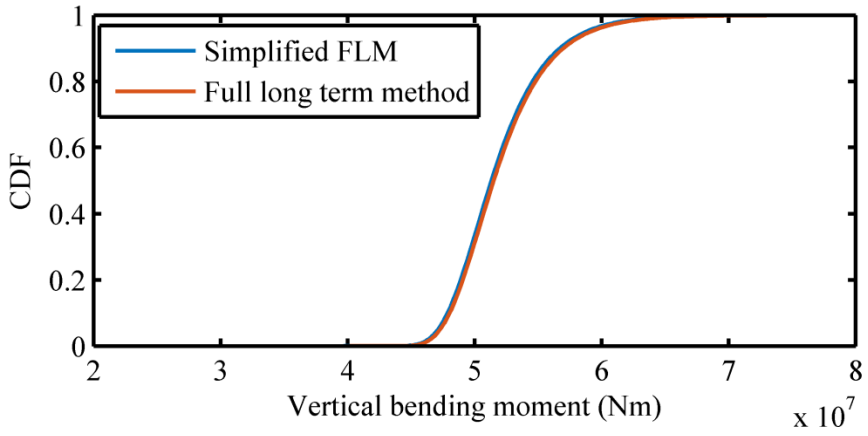

Fig. 13 Comparison of the distributions of the extreme bending moment in 100 years obtained using the FLM and the simplified FLM as defined in Table 2

4.5 Environmental contour method

(1) ECM based on the frequency domain results

Fig. 14 shows the environmental contour surface for 100-yr-return environmental conditions. The short-term extreme value distribution for 63×63 cases on the surface are calculated based on Eq. (40). The red point in the figure shows the position of the case that yields the largest median extreme value of the bending moment due to vertical deformation. The blue lines represent the slice of the contour surface at V=30.67 m/s and T_p=8 s.

The short-term extreme value distribution for the most important case is compared with the full long-term extreme value distribution (Fig. 15). The correction factor α is defined as the ratio between an

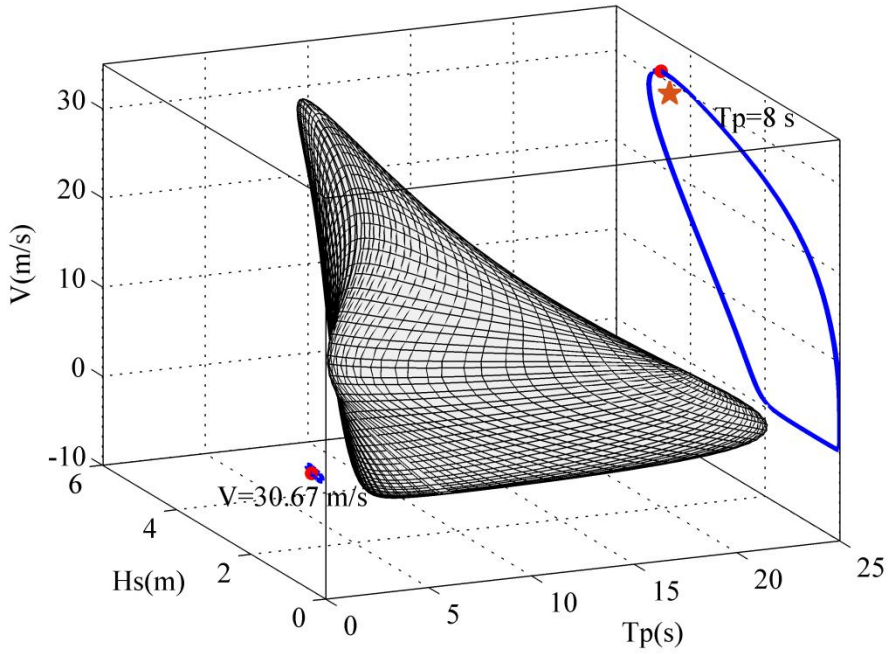

Fig. 14 Environmental contour surface for 100-yr-return period.. The • symbol denotes the most important condition on the contour surface, and the ★ symbol represents the design point found in the IFORM

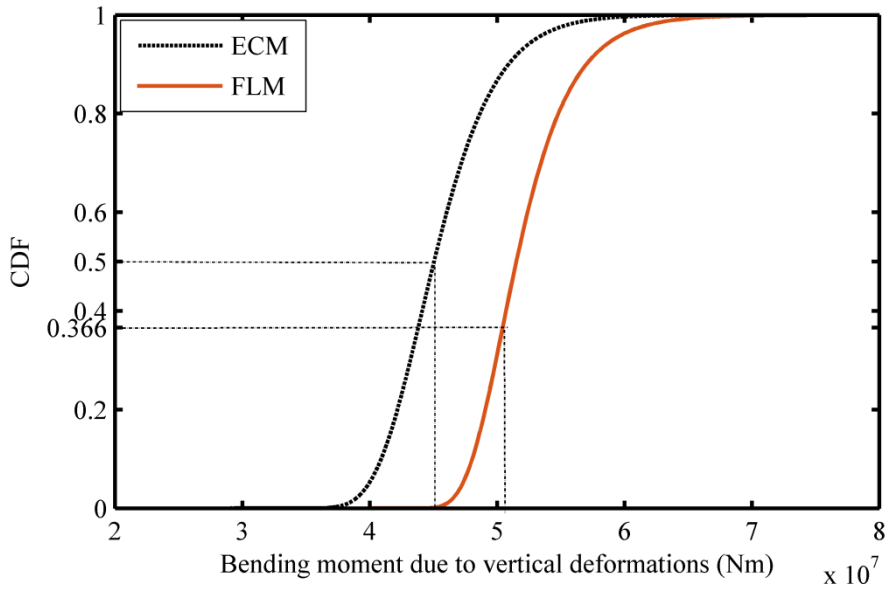

Fig. 15 Comparison of the short-term and full long-term extreme value distributions obtained from the ECM

annual probability value of 10^{-2} based on the FLM (50.43 MNm) and the median short-term extreme value (45.05 MNm):

$$\alpha = \frac{50.43 MNm}{45.05 MNm} \approx 1.12$$

The 10^{-2} annual probability value is obtained from the long-term extreme value distribution as the CDF is $(1-10^{-2})^{100}=0.366$.

(2) ECM based on time domain simulations

Evaluating many environmental conditions along the contour surface requires too much computational effort when it is necessary to simulate the response in time domain. Fig. 9 shows the dynamic response of the structure when nonlinear effects are included and disregarded. The curves are similar in the sense that it is only the peak values that are slightly changed while the overall characteristics of the response remain the same when including the nonlinear effects. This indicates that the system is only weakly nonlinear, which makes it reasonable to assume that the location of the most important region does not change significantly. Ten realizations of the most important case, which were discovered based on the abovementioned frequency domain results, are therefore simulated using the time domain method. Since this time domain approach represents a weakly nonlinear dynamic problem, it is reasonable to assume that the most important case on the environmental contour surface and the correction factor are the same as those when considering nonlinear effects. The curve fitting results of

the ACER function and the short-term extreme value distribution in consideration of nonlinearities have been shown in Fig. 11. The median extreme value for the 1-h extreme value is 54.3 MNm. Multiplying this value by α =1.12, which is assumed to be the same for the linear and nonlinear systems, the 100-yr extreme value is found to be 60.8 MNm.

4.6 IFORM

(1) IFORM based on the frequency domain results

The ECM ignores the variability in the short-term extreme values and assumes that the standard Gaussian variable corresponding to the short-term extreme value is zero. The value of this Gaussian variable fluctuates for different dynamic problems, and it is usually larger than zero. Therefore, the design case found using the IFORM (V=28.7 m/s, H_s=4.57 m and T_p=8 s) is usually located on the inside of the contour surface, and it is represented by a star in Fig. 14. With an increasing importance of the variability in the short-term extreme value, the design point will be located increasingly toward the interior of the contour surface. The accuracy of the predicted extreme bending moment based on the IFORM (51.54 MNm) is validated through a comparison with the FLM (50.43 MNm). The difference for this case is:

$$\frac{51.54-50.43}{50.43}=2.2\%.$$

(2) IFORM based on the combined frequency and time domain results

Both ‘exact’ and approximate approaches can be used to implement the IFORM based on the combined frequency and time domain simulation results. With the ‘exact’ approach, the time domain simulations are processed during each iteration of searching for the MPP to calculate the gradient of the limit state function $g(\mathbf{u}^k)$. Assuming that this process requires 8 iterations before the IFORM

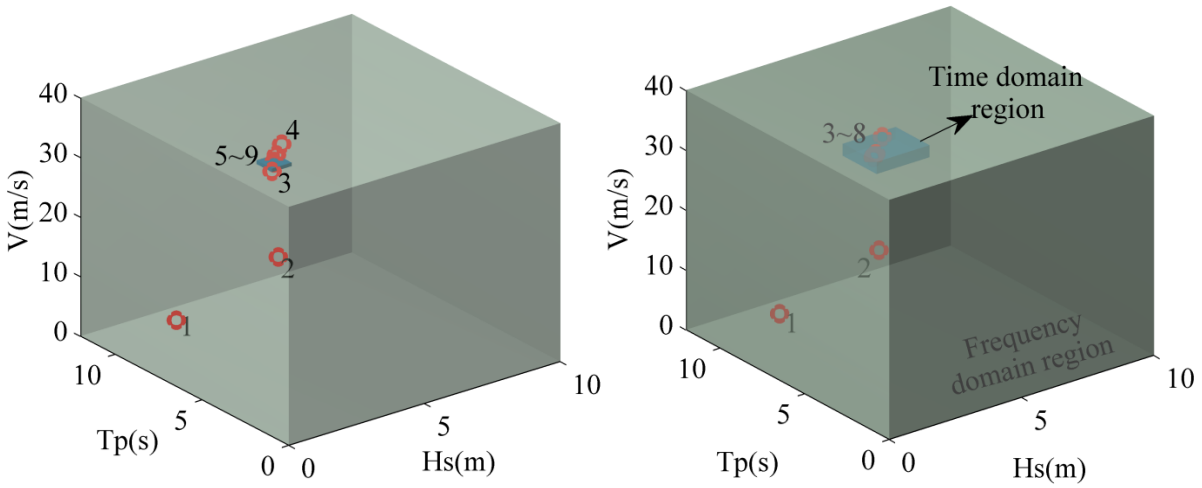

Fig. 16 Iterations of the IFORM based on a) the frequency domain results and b) the combination of the frequency and time domain results

converges and that the time domain simulations require 12 h for each iteration in this case study, the 'exact' approach needs 96 h to determine each response parameter since the maximum of different parameters don't necessarily occur at the same time, e.g., the section force in the girder or the axial force in the cables or tethers. In the approximate approach, the time domain simulations are accomplished prior to the iterations in the IFORM. However, not all of the potential environmental conditions must be simulated within the time domain approach because most of the iterations are concentrated in a very small space ($28.5<V<29.1$ m/s, $4.18<H_s<4.93$ m and $7.5<T_p<8.4$ s), as indicated by the frequency domain results (blue area in Fig. 16(a)). Considering that this is a weakly nonlinear dynamic problem, the design case will not change significantly. Therefore, only the environmental conditions around the design conditions are simulated in the time domain approach in consideration of nonlinearities (i.e., $28<V<30$ m/s, $4<H_s<6$ m and $7<T_p<9$ s), as shown by the blue space in Fig. 16(b). During each iteration, the gradient of the limit state function is calculated based on the frequency domain method if the condition is located in the green area. When the iteration enters the blue space, the gradient will be calculated using the linear interpolation of the pre-calculated time domain results. Thus, the time domain simulations can be conducted in parallel instead of in series as in the 'exact' approach. Furthermore, it is unnecessary to rerun the time domain simulations when predicting the long-term extremes values for different response parameters.

In this case study, wherein the extreme value of the bending moment due to vertical deformation in the bridge girder is predicted, the first 2 iterations are processed based on the frequency domain results while the final 6 iterations are accomplished based on the time domain results. The design condition obtained is V=28.9 m/s, H_s=4.63 m and T_p=8.04 s, which is in the time-domain region and is very close to that found using IFORM based on the frequency-domain results. The characteristic 100 yr extreme value is X_{crit}=62.0 MNm. Comparison to the results obtained based on the other methods are listed in Table 3.

Table 3 Comparison of the 100 yr extreme values of the bending moment based on different methods

Method	Extreme response value based on FD results (MNm)	Extreme response value based on FD&TD results (MNm)
FLM	50.43	/
Simplified FLM	50.26	/
ECM	49.56~58.57	60.8
IFORM	51.54	62

5. Conclusions

This paper presents a study of multiple efficient approaches, i.e., the simplified FLM, the ECM and the IFORM, used to predict the long-term extreme load effects due to combined wave and wind load on a cable-supported bridge with floating pylons. This research was conducted because a comparison of the results obtained using frequency and time domain approaches revealed that nonlinearities can constitute a difference of approximately 20% in the extreme values of the bending moment due to vertical deformation at the most important position along the girder. The findings presented herein indicate that the structural dynamic response should be solved in the time domain to consider nonlinear effects. However, time domain simulations can require tremendous computational times to predict the long-term extreme value distribution.

Relative to the FLM, the simplified FLM can predict equally accurate extreme values while requiring approximately 10 times less computational effort. However, the number of environmental conditions required is still very large, and thus, the simplified FLM is not an effective choice for this case study if the conditions must be simulated in the time domain.

The ECM is the most efficient approach. The most important condition on the contour surface for N-year-return environmental conditions and the correction factor can be obtained based on the frequency domain results. It is reasonable to assume that the most important case and the correction factor are the same when considering nonlinear effects since this is a weakly nonlinear dynamic problem.

The IFORM can accurately predict the extreme values of the bending moment with an error of approximately 2.2% for this case study based on the frequency domain results. In order to include the nonlinear effects and to save computational time, the frequency domain and time domain results are combined in the IFORM iterations. The domain of environmental parameters is divided into a frequency domain region and a time domain region. Time domain simulations are performed only as the iteration is located in the time domain region. Since most of the IFORM iterations are concentrated in a very small space that is centered around the design case, the time domain region constitutes only a small percentage of the domain, which is the key to avoid tremendous computational time.

Comparing the performance of these three approximate approaches in the prediction of long-term extreme load effects due to wave and wind actions, the IFORM based on combined frequency- and time-domain results is most recommended for this particular case. The simplified FLM is not recommended since it still requires tremendous time-domain simulations. The ECM requires the least time-domain simulations, but the assumption that the design condition and correction factor do not change when considering the nonlinearities cannot be proved. Although it is also assumed in IFORM that the design condition is in the enlarged time-domain region determined based on the frequency-domain results, this assumption have been proved satisfied in this case study.

Acknowledgments

This research was conducted with financial support from the Norwegian Public Roads Administration. The authors gratefully acknowledge this support.

References

[1] NORSOK Standard N-003: Actions and action effects. Standards Norway, Lysaker; 2007.
[2] Sagrilo LVS, Naess A, Doria AS. On the long-term response of marine structures. Applied Ocean Research. 2011;33:208-14.

[3] Naess A, Moan T. Stochastic dynamics of marine structures: Cambridge University Press; 2012.
[4] Ditlevsen O. Principle of normal tail approximation. Journal of the Engineering Mechanics Division. 1981;107:1191-208.
[5] Rackwitz R, Flessler B. Structural reliability under combined random load sequences. Computers & Structures. 1978;9:489-94.
[6] Zhao Y-G, Ono T. A general procedure for first/second-order reliabilitymethod (form/sorm). Structural safety. 1999;21:95-112.
[7] Der Kiureghian A, Zhang Y, Li C-C. Inverse reliability problem. Journal of engineering mechanics. 1994;120:1154-9.
[8] Li H, Foschi RO. An inverse reliability method and its application. Structural Safety. 1998;20:257-70.
[9] Winterstein SR, Ude TC, Cornell CA, Bjerager P, Haver S. Environmental parameters for extreme response: Inverse FORM with omission factors. Proc 6th Int Conf on Structural Safety and Reliability, Innsbruck, Austria1993.
[10] Haver S, Kleiven G. Environmental Contour Lines for Design Purposes: Why and When? ASME 2004 23rd International Conference on Offshore Mechanics and Arctic Engineering: American Society of Mechanical Engineers; 2004. p. 337-45.
[11] Haver S, Winterstein SR. Environmental contour lines: A method for estimating long term extremes by a short term analysis. Transactions of the Society of Naval Architects and Marine Engineers. 2009;116:116-27.
[12] Saranyasoontorn K, Manuel L. Design loads for wind turbines using the environmental contour method. Journal of Solar Energy Engineering. 2006;128:554-61.
[13] Li Q, Gao Z, Moan T. Modified environmental contour method for predicting long-term extreme responses of bottom-fixed offshore wind turbines. Marine Structures. 2016;48:15-32.
[14] Haver SK. Prediction of Characteristics Response for Design Purposes. StatoilHydro; 2007.
[15] Li Q, Gao Z, Moan T. Modified environmental contour method to determine the long-term extreme responses of a semi-submersible wind turbine. Ocean Engineering. 2017;142:563-76.
[16] Xu Y, Øiseth O, Moan T. Time Domain Modelling of Frequency Dependent Wind and Wave Forces on a Three-Span Suspension Bridge With Two Floating Pylons Using State Space Models. ASME 2017 36th International Conference on Ocean, Offshore and Arctic Engineering: American Society of Mechanical Engineers; 2017.
[17] Xu Y, Øiseth O, Moan T. Time domain simulations of wind-and wave-induced load effects on a three-span suspension bridge with two floating pylons. Marine Structures. 2018;58:434-52.
[18] Chen X, Matsumoto M, Kareem A. Aerodynamic coupling effects on flutter and buffeting of bridges. Journal of Engineering Mechanics. 2000;126:17-26.
[19] Chen X, Kareem A, Matsumoto M. Multimode coupled flutter and buffeting analysis of long span bridges. Journal of Wind Engineering and Industrial Aerodynamics. 2001;89:649-64.
[20] Scanlan RH, Tomko J. Air foil and bridge deck flutter derivatives. Journal of Soil Mechanics & Foundations Div. 1971;97:1717-37.
[21] Øiseth O, Rönnquist A, Sigbjörnsson R. Simplified prediction of wind-induced response and stability limit of slender long-span suspension bridges, based on modified quasi-steady theory: a case study. Journal of wind engineering and industrial aerodynamics. 2010;98:730-41.
[22] Faltinsen O. Sea loads on ships and offshore structures: Cambridge university press; 1993.
[23] Longuet-Higgins M, Cartwright DE, Smith ND. Observations of the directional spectrum of sea waves using the motions of a floating buoy. Ocean Wave Spectra, proceedings of a conference, Easton, Maryland: Prentice-Hall; 1963. p. 111-36.
[24] Taghipour R, Perez T, Moan T. Hybrid frequency–time domain models for dynamic response analysis of marine structures. Ocean Engineering. 2008;35:685-705.
[25] Chen X, Kareem A. Aeroelastic Analysis of Bridges under Multicorrelated Winds: Integrated State-Space Approach. Journal of Engineering Mechanics. 2001;127:1124-34.
[26] Chen X, Kareem A. Advances in modeling of aerodynamic forces on bridge decks. Journal of Engineering Mechanics. 2002;128:1193-205.
[27] Chen X, Matsumoto M, Kareem A. Time Domain Flutter and Buffeting Response Analysis of Bridges. Journal of Engineering Mechanics. 2000;126:7-16.

[28] Øiseth O, Rönnquist A, Sigbjörnsson R. Finite element formulation of the self-excited forces for time-domain assessment of wind-induced dynamic response and flutter stability limit of cable-supported bridges. Finite Elements in Analysis and Design. 2012;50:173-83.
[29] Xu Y, Øiseth O, Naess A, Moan T. Prediction of long-term extreme load effects due to wind for cable-supported bridges using time-domain simulations. Engineering Structures. 2017;148:239-53.
[30] Strømmen E. Theory of bridge aerodynamics. 2 ed: Springer Science & Business Media; 2010.
[31] Sharma JN, Dean RG. Second-Order Directional Seas and Associated Wave Forces. Society of Petroleum Engineers Journal. 1981:129-40.
[32] Rosenblatt M. Remarks on a Multivariate Transformation. Ann Math Statist. 1952;23:470-2.
[33] Du X. First order and second reliability methods. In: Probabilistic Engineering Design. University of Missouri. 2005.
[34] Giske F-IG, Leira BJ, Øiseth O. Long-term extreme response analysis of marine structures using inverse SORM. ASME 2017 36th International Conference on Ocean, Offshore and Arctic Engineering: American Society of Mechanical Engineers; 2017.
[35] Nocedal J, Wright S. Numerical Optimization. 2 ed: Springer-Verlag New York; 2006.
[36] Kleiven G, Haver S. Met-ocean contour lines for design; correction for omitted variability in the response process. The Fourteenth International Offshore and Polar Engineering Conference: International Society of Offshore and Polar Engineers; 2004.
[37] Gong SW, Halden S. Dynamic Response of Suspension Bridge with Floating Towers. Master thesis; Department of Structural Engineering, NTNU; 2016.
[38] Hibbitt, Karlsson, Sorensen. ABAQUS/Standard user's manual: Hibbitt, Karlsson & Sorensen; 2001.
[39] Lee C-H. WAMIT theory manual: Massachusetts Institute of Technology, Department of Ocean Engineering; 1995.
[40] Johannessen K, Meling TS, Hayer S. Joint distribution for wind and waves in the northern north sea. International Journal of Offshore and Polar Engineering. 2002;12.
[41] Li L, Gao Z, Moan T. Joint distribution of environmental condition at five European offshore sites for design of combined wind and wave energy devices. Journal of Offshore Mechanics and Arctic Engineering. 2015;137:031901.
[42] Naess A, Gaidai O. Estimation of extreme values from sampled time series. Structural Safety. 2009;31:325-34.